Observation and Manipulation of Chiral Phasons in a Magnetic System

Shilei Zhang

shilei.zhang@shanghaitech.edu.cn

ShanghaiTech University https://orcid.org/0000-0002-6870-9222

Yang Wu

ShanghaiTech University

Zhang Chenhao

ShanghaiTech University https://orcid.org/0009-0003-2982-2729

Jingyi Chen

ShanghaiTech University

Haonan Jin

ShanghaiTech University

Gerrit van der Laan

Diamond Light Source https://orcid.org/0000-0001-6852-2495

Thorsten Hesjedal

University of Oxford https://orcid.org/0000-0001-7947-3692

Yizhou Liu

High Magnetic Field Laboratory, HFIPS, Chinese Academy of Sciences https://orcid.org/0000-0002-0760-4179

Jiadong Zang

University of New Hampshire https://orcid.org/0000-0002-5089-9806

Xiao-Ping Liu

Shanghai Tech University

Article

Keywords:

Posted Date: July 30th, 2025

DOI: https://doi.org/10.21203/rs.3.rs-7058774/v1

Additional Declarations: There is **NO** Competing Interest.

Observation and Manipulation of Chiral Phasons in a Magnetic System

Yang Wu*,[1,2] Chenhao Zhang*,[1] Jingyi Chen*,[1,2] Haonan Jin†,[1,2] Gerrit van der Laan,[3] Thorsten Hesjedal,[4] Yizhou Liu,[5] Jiadong Zang,[6] Xiaoping Liu†,[1,2] and Shilei Zhang†[1,2,7]

[1]*School of Physical Science and Technology, ShanghaiTech University, Shanghai 201210, China*

[2]*ShanghaiTech Laboratory for Topological Physics, ShanghaiTech University, Shanghai 201210, China*

[3]*Magnetic Spectroscopy, Diamond Light Source, Harwell Science and Innovation Campus, Didcot OX11 0DE, United Kingdom*

[4]*Department of Physics, Clarendon Laboratory, University of Oxford, Oxford OX1 3PU, United Kingdom*

[5]*Anhui Province Key Laboratory of Low-Energy Quantum Materials and Devices, High Magnetic Field Laboratory, HFIPS, Chinese Academy of Sciences, Hefei 230031, China*

[6]*Department of Physics and Astronomy, University of New Hampshire, Durham, NH, 03824, USA*

[7]*Center for Transformative Science, ShanghaiTech University, Shanghai 200031, China*

Phasons [1–6], quasiparticle excitations corresponding to phase shifts in incommensurate orders, represent the lowest-energy Goldstone modes of such systems, yet have remained unobserved in magnetic materials. Here, we activate the Goldstone mode of a one-dimensional chiral spin helix in a helimagnet by exploiting nonlinear spin dynamics, revealing an Archimedean screw [7] phason mode at megahertz frequencies. This unique phase-sliding behavior is directly evidenced through a Doppler-shift signature detected via stroboscopic magneto-optical Kerr effect measurements. Remarkably, owing to the intrinsic screw symmetry of the system, forward- and backward-propagating phasons can be selectively excited, demonstrating well-defined mode chirality. Our results unveil a novel pumping mechanism in magnetic materials and establish a tunable experimental platform for the study of Floquet magnetism.

In commensurate electronic orders arise from competing microscopic interactions among multiple energy scales, a phenomenon ubiquitous in condensed matter systems [8]. These long-wavelength modulations are typically decoupled from the underlying crystal lattice, rendering the modulation phase a free parameter. As a result, the system hosts a fundamental, lowest-energy Goldstone excitation. This *phason* corresponds to continuous phase-sliding dynamics, whereby the entire ordered pattern translates collectively in real space [1–6]. However, in real materials, these low-energy excitations are typically suppressed by intrinsic or extrinsic pinning potentials [1–3], making the experimental creation and detection of phasons exceptionally challenging, and, to date, elusive in magnetic systems.

A promising route to realizing phason excitations in magnetic systems lies in noncentrosymmetric materials, where the weaker Dzyaloshinskii–Moriya interaction (DMI) competes energetically with the stronger Heisenberg exchange [9–13]. At elevated static magnetic field $\mathbf{H}_{\mathrm{dc}}$, these systems stabilize an incommensurate conical spin order as the ground state, with the helical wavevector $\mathbf{q}_h$ aligned along the field direction [14, 15]. Assuming $\mathbf{q}_h \parallel z$, the normalized conical spin texture is given by $\mathbf{m}_0(z) = \sin\eta\cos(q_h z + \phi)\,\hat{n}_x + \sin\eta\sin(q_h z + \phi)\,\hat{n}_y + \cos\eta\,\hat{n}_z$, where η is the cone angle and ϕ is the spatial phase of the helical chain. As illustrated in Fig. 1a, in the absence of pinning, the phase ϕ is arbitrary, i.e., shifting the helicoid configuration from ϕ to $\phi + \delta\phi$ incurs no energy cost [13, 15]. This spontaneous breaking of continuous $U(1)$ symmetry thus gives rise to a Goldstone mode, whose excitation corresponds to a phase-sliding dynamics $\phi(t)$ [7, 16].

Although such 'hidden' dynamics has not yet been experimentally observed, it has been theoretically predicted that, in a conical spin order, the phason excitation is dynamically coupled to one of the system's magnon eigenmodes [7]. In other words, by resonantly exciting the system into its intrinsic spin-wave mode, namely the $+\mathcal{Q}$ or $-\mathcal{Q}$ helimagnon branch [17–19], the global phase ϕ can be continuously shifted as a secondary (parasitic) effect, occurring at a much lower frequency. Remarkably, owing to the screw symmetry of the spin helix, this phason propagation is inherently non-reciprocal: excitation into the $-\mathcal{Q}$ ($+\mathcal{Q}$) mode drives ϕ to translate forward (backward) in real space. As visualized in Supplementary Movies 1 and 2, the resulting unidirectional phase motion corresponds to a collective rotation of the entire conical spin chain, reminiscent of transport via an Archimedean screw. Thus, the Goldstone mode of a conical magnetic order manifests as a novel type of chiral phason.

Here, we demonstrate that such chiral phasons can be both created and observed in

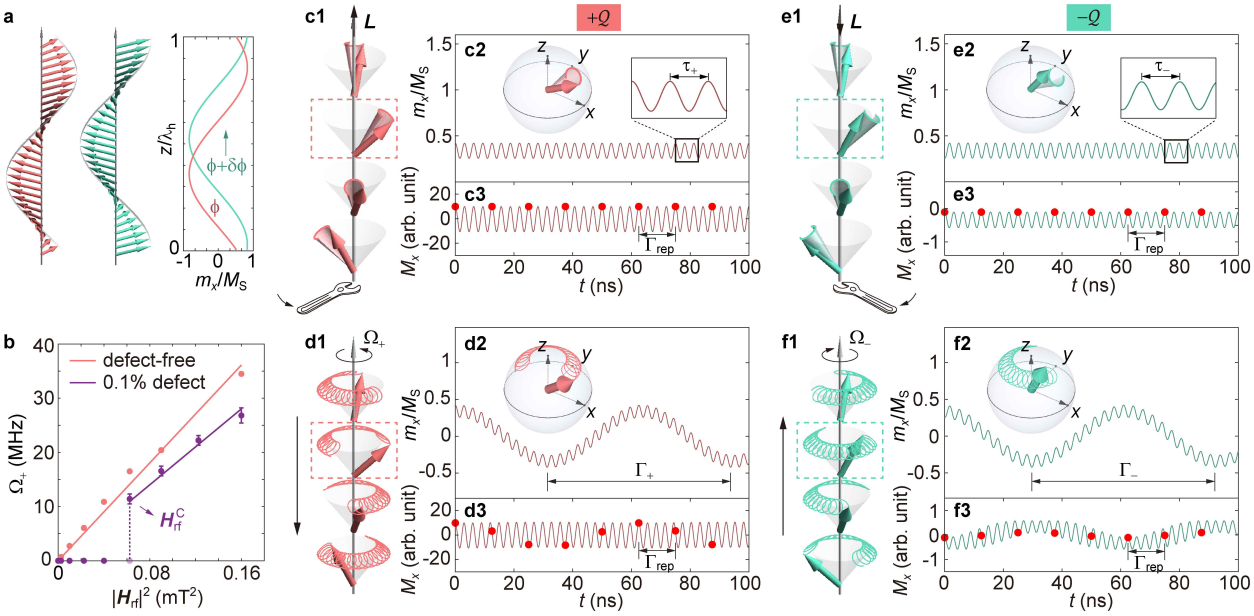

FIG. 1. **Excitation of chiral phasons in a conical spin order.** **a**, The choice of the spatial phase ϕ in a helicoidal spin structure corresponds to the spontaneous breaking of $U(1)$ symmetry, indicating the existence of a phason excitation, i.e., $\phi \to \phi + \delta\phi$. **b**, Calculated phason frequency Ω_+ as a function of microwave driving power $|\mathbf{H}_{\rm rf}|^2$ for an ideal, defect-free Cu_2OSeO_3 crystal (red curve), and for a system with 0.1% pinning centers (purple curve). **c**, For $|\mathbf{H}_{\rm rf}| < H_{\rm rf}^{\rm C}$, the magnon resonance at the $+\mathcal{Q}$ mode results in stationary spin precession at frequency ω_+, as illustrated by the m_x component dynamics of an individual spin (highlighted by the red box). This leads to a real-time magnetization response $M_x(t)$ oscillating with a periodicity of $\tau_+ = 1/\omega_+$. The red dots indicate the stroboscopic sampling points, spaced by a repetition period $\Gamma_{\rm rep} = m\tau_+$, where m is an integer. **d**, Once $|\mathbf{H}_{\rm rf}| \geq H_{\rm rf}^{\rm C}$, the spins not only precess at ω_+ but also undergo counterclockwise gyration around the z-axis at frequency Ω_+, resulting in an Archimedean screw-like motion that translates the entire conical chain along $-z$. The corresponding m_x dynamics acquires a low-frequency modulation with periodicity $\Gamma_+ = 1/\Omega_+$. As a result, $M_x(t)$ exhibits a Doppler-shifted frequency $\omega_+ + \Omega_+$, producing an aliased pattern in the stroboscopic measurement. **e,f**, Same as **c,d**, but for the $-\mathcal{Q}$ mode, which activates a forward-sliding phason.

Cu_2OSeO_3, specifically that forward- and backward-sliding modes can be selectively activated and dynamically controlled. Moreover, we quantitatively determine their propagation frequencies and threshold conditions for excitation. The observed conical Archimedean screw effect introduces Floquet characteristics into both magnonic and electronic eigenstates [7, 20]. In addition, it establishes a 'magnon laser' regime, wherein giant-amplitude magnetization density waves propagate coherently along the helical axis.

Figure 1 illustrates the activation mechanism for low-frequency chiral phasons. A GHz-range microwave field $\mathbf{H}_{\rm rf}$ ($\perp \mathbf{H}_{\rm dc}$) with frequency ω_+ (ω_-), is applied to the conical spin helix, driving the system into the $+\mathcal{Q}$ ($-\mathcal{Q}$) magnon mode [21, 22]. As shown in Fig. 1c1 and 1e1, at $\pm\mathcal{Q}$ resonance, the spins $\mathbf{m}(z,t)$ precess around their local equilibrium configuration

$\mathbf{m}_0(z)$ with a periodicity $\tau_\pm = 1/\omega_\pm$. Crucially, the dynamical phase of the spin precession increases (for $+\mathcal{Q}$) or decreases (for $-\mathcal{Q}$) along the z-axis [19, 21, 22], creating a temporal phase gradient. This gradient induces a net torque on the conical chain, generating a collective angular momentum $\mathbf{L}$ along z. As a result, during magnon resonance, the precessing spins also undergo a slow, secular rotation at frequency $\Omega_\pm$, tracing out gyration trajectories as shown in Fig. 1d,f. Specifically, Ω_+ corresponds to counterclockwise gyration, resulting in a backward-sliding phason mode, while Ω_- leads to clockwise gyration and a forward-sliding mode.

It is worth noting that chiral phasons are exceptionally soft modes, emerging only as second-order responses to the rf drive. Accordingly, $\Omega_\pm$ does not correspond to an intrinsic eigenfrequency, but instead scales quadratically with the microwave field amplitude, i.e., $\Omega_\pm \propto |\mathbf{H}_{\rm rf}|^2$ [7]. Figure 1b (red curve) shows the calculated phason frequency Ω_+ as a function of microwave power for an ideal, defect-free Cu_2OSeO_3 model. The system remains gapless, and once the $+\mathcal{Q}$ magnon mode is excited, the conical structure immediately begins to drift along $-z$. For experimentally accessible values of $|\mathbf{H}_{\rm rf}|$, the resulting Ω lies in the few-MHz range, corresponding to an ultra-low energy scale.

In practical materials, phason dynamics are strongly influenced by defect-induced pinning potentials [2, 3, 7]. The purple curve in Fig. 1b illustrates the Ω_+ vs. $|\mathbf{H}_{\rm rf}|^2$ relation for the same Cu_2OSeO_3 system in the presence of a finite defect density. At low microwave amplitudes, below a threshold value $H_{\rm rf}^{\rm C}$, the phason motion is pinned by these energy barriers. In this regime, the system exhibits only high-frequency spin precession at the magnon resonance, while the conical lattice remains static, as shown in Fig. 1c2. However, once the input power exceeds $H_{\rm rf}^{\rm C}$, the Archimedean screw-like sliding motion of the conical structure is triggered (see Fig. 1d2), and the phason frequency resumes its quadratic dependence on the microwave amplitude.

Next, we examine the macroscopic characteristics of chiral phasons. A particularly useful quantity is the real-time magnetization response, defined as $M_x(t) = \int_z m_x(z,t)\, dz$. If a sufficiently large number of spins are sampled from the conical chain, M_x is nearly zero in the static state due to spatial averaging. When a microwave drive at frequency ω_+ is applied with amplitude $|\mathbf{H}_{\rm rf}| < H_{\rm rf}^{\rm C}$, the system enters the stationary $+\mathcal{Q}$ magnon mode, where $\Omega_+ = 0$ (see Fig. 1c1 and 1c2). Under these conditions, $M_x(t)$ exhibits a non-zero oscillation at the driving frequency ω_+, as shown in Fig. 1c3. This stationary modulation

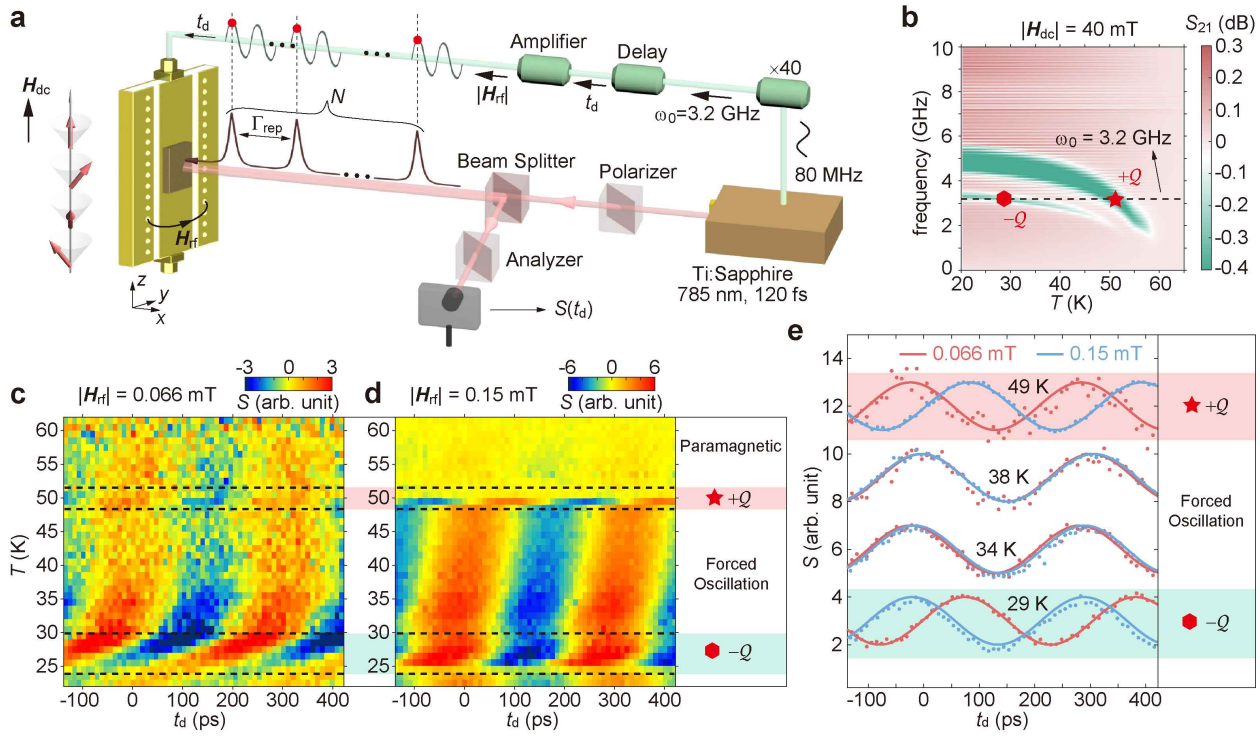

FIG. 2. **Experimental evidence for the existence of chiral phasons.** **a**, Stroboscopic MOKE setup. Pink lines represent the laser beam paths, while green lines indicate the microwave circuit. The timing structures of the laser pulses and the synchronized microwave signal are illustrated. Here, $\Gamma_{\rm rep} = 12.5$ ns, $N = 64{,}673$, and the microwave frequency is fixed at 3.2 GHz. **b**, VNA-detected spin resonance spectrum measured at varying temperatures, with $|\mathbf{H}_{\rm dc}|$ held constant at 40 mT. At $\omega_0 = 3.2$ GHz, resonance temperatures for the $+\mathcal{Q}$ and $-\mathcal{Q}$ modes are identified as $T_+ \approx 49$ K and $T_- \approx 28$ K, respectively. **c**, Following the scanning trajectory marked by the dashed line in (B), stroboscopic MOKE signals $S(t_d)$ are measured at $|\mathbf{H}_{\rm dc}| = 40$ mT and $|\mathbf{H}_{\rm rf}| = 0.066$ mT across varying temperatures. **d**, Upon increasing $|\mathbf{H}_{\rm rf}|$ to 0.15 mT, phase drifts emerge in the $S(t_d)$ map at T_+ and T_-, indicating the onset of phason motion. Note that $t_d = 0$ corresponds to the red dots on the microwave pulse train line in panel **a**, denoting the start of the time delay. **e**, Comparison of the $S(t_d)$ profiles under sub-threshold ($|\mathbf{H}_{\rm rf}| < H_{\rm rf}^C$, red) and super-threshold ($|\mathbf{H}_{\rm rf}| > H_{\rm rf}^C$, blue) conditions at representative temperatures. The data are normalized, vertically offset, and fitted with sinusoidal functions to highlight relative phase differences.

can be analyzed using stroboscopic sampling. For instance, the red dots in Fig. 1c3 indicate sampling points spaced by a repetition period $\Gamma_{\rm rep}$, chosen as an integer multiple of τ_+. Consequently, all sampling points are in-phase with the underlying magnetization profile, capturing the spin precession dynamics.

In contrast, when $|\mathbf{H}_{\rm rf}|$ is increased beyond the phason threshold $H_{\rm rf}^{\rm C}$, the conical chain begins to slide along the $-z$ direction with frequency Ω_+, as shown in Fig. 1d1 and 1d2. As a result, although $M_x(t)$ retains a well-defined sinusoidal form, its frequency is shifted to $\omega_+ + \Omega_+$, an effect analogous to a Doppler shift [23]. In this case, as illustrated in Fig. 1d3, stroboscopic sampling under the same $\Gamma_{\rm rep}$ results in an aliasing pattern due to the

slight mismatch between the sampling rate and the shifted signal frequency. An identical phenomenon occurs for the $-\mathcal{Q}$-induced forward-sliding phason, as shown in Fig. 1e,f. Thus, an $|\mathbf{H}_{\rm rf}|$-dependent Doppler shift in the $M_x(t)$ response serves as a key experimental signature that uniquely identifies the presence of phason excitations.

To experimentally resolve the Doppler shift in $M_x(t)$, we employ stroboscopic magneto-optical Kerr effect (MOKE) measurements at low temperatures. Figure 2a illustrates the experimental setup and underlying measurement principle. A 100-μm-thick Cu_2OSeO_3 single crystal is mounted on top of a cryostat-compatible coplanar waveguide. A static magnetic field $\mathbf{H}_{\rm dc}$ is applied along the z-axis, while the rf field $\mathbf{H}_{\rm rf}$ is oriented along y. Transient polar MOKE [24] is implemented using a Ti:sapphire laser (wavelength: 785 nm, pulse width: 120 fs), which is sensitive to the instantaneous M_x component of the magnetization. The time structure of the laser pulse train, shown in Fig. 2a, features a repetition rate of 80 MHz, corresponding to a sampling interval $\Gamma_{\rm rep} = 12.5$ ns. Using a fast lock-in detection scheme [25], the measured stroboscopic signal, denoted as S, is obtained by integrating the instantaneous MOKE response over N laser pulses, with $N = 64{,}673$ for the present experiment. Thus, when the system exhibits a time-dependent $M_x(t)$ response, the stroboscopic signal is given by $S = \sum_{n=1}^{N} M_x(n\Gamma_{\rm rep})$.

Meanwhile, the intrinsic 80 MHz laser repetition rate is used to generate a single-harmonic, time-synchronized continuous-wave microwave field at $\omega_0 = 3.2$ GHz. This $\mathbf{H}_{\rm rf}$ field is phase-locked to the laser pulses and drives the system into one of the two magnon eigenmodes. A variable time delay t_d between the sinusoidal microwave and the laser strobe pulses can be precisely controlled. By continuously scanning the stroboscopic signal $S(t_d)$, time-domain information on the spin dynamics can be extracted. Additionally, the microwave amplitude $|\mathbf{H}_{\rm rf}|$ can be continuously tuned, enabling controlled activation of the chiral phason modes.

Next, we discuss the relationship between the real-time magnetization $M_x(t)$ and the measured stroboscopic signal $S(t_d)$. For the conical spin dynamics, the magnetization follows [25]:

$$M_x(t) = \mathcal{A}_{\pm} \cos\left[2\pi(\omega_0 \pm \Omega_{\pm})t + \phi_{\pm}\right], \tag{1}$$

where $\mathcal{A}_{\pm}$ is the amplitude of the ac susceptibility for the $\pm\mathcal{Q}$ magnon mode and scales with the spin precession cone angle. $\phi_{\pm}$ denotes the phase of the ac response, governed by the static conical phase ϕ. The frequency shift $\Omega_{\pm}$ accounts for the Doppler effect

introduced by the propagating phason. Accordingly, the stroboscopic signal is given by $S(t_d) = \sum_{n=1}^{N} M_x(n\Gamma_{\text{rep}} + t_d)$, which evaluates to the analytic expression:

$$S(t_d) = \mathcal{Y} \cos\left[2\pi(\omega_0 \pm \Omega_\pm)t_d + (N+1)\pi(\omega_0 \pm \Omega_\pm)\Gamma_{\text{rep}} + \phi_\pm\right] \quad , \tag{2}$$

where $\mathcal{Y}$ is a prefactor that depends on N [25].

As indicated by equation (1), if $\Omega_\pm = 0$, the magnetization $M_x(t)$ oscillates at the same frequency as the microwave drive, reducing to $M_x(t) \approx \cos(2\pi\omega_0 t + \phi_\pm)$. Accordingly, the stroboscopic signal becomes $S(t_d) \approx \mathcal{Y}\cos(2\pi\omega_0 t_d + \phi_\pm)$. In other words, when the phason sliding motion is not activated, the measured $S(t_d)$ waveform fully reproduces the underlying magnetization dynamics. Its phase remains constant and independent of the driving amplitude $|\mathbf{H}_{\text{rf}}|$.

In stark contrast, once a chiral phason is excited, a non-zero $\Omega_\pm$ emerges, resulting in a Doppler shift in the $M_x(t)$ signal. As shown in equation (3), this shift induces an aliasing effect in the stroboscopic detection, producing a phase variation in the measured $S(t_d)$ signal that depends on $\Omega_\pm$. This behavior forms the basis of our experimental strategy for identifying and characterizing phason excitations. In principle, at the $\pm\mathcal{Q}$ resonance, if the phase of the $S(t_d)$ modulation remains constant with increasing microwave amplitude $|\mathbf{H}_{\text{rf}}|$, one can infer that $\Omega_\pm = 0$. Conversely, a measurable phase drift in $S(t_d)$ with varying $|\mathbf{H}_{\text{rf}}|$ confirms the onset of the Archimedean screw mode. The corresponding $\Omega_\pm$ can then be quantitatively extracted by fitting the $S(t_d)$ data using equation (3).

We first identify the spin resonance conditions for the $\pm\mathcal{Q}$ modes using frequency-domain spectroscopy. Figure 2b presents the magnon absorption map acquired with a vector network analyzer (VNA), performed *in situ* prior to the time-domain MOKE measurements. At a fixed static field of $|\mathbf{H}_{\text{dc}}| = 40$ mT, the microwave transmission parameter S_{21} is recorded as a function of driving frequency and temperature. The $+\mathcal{Q}$ and $-\mathcal{Q}$ magnon modes appear as two distinct absorption branches, consistent with previous reports [21, 22, 26]. The dashed line in Fig. 2b indicates the microwave frequency $\omega_0 = 3.2$ GHz, which is employed in the subsequent stroboscopic measurements. At this frequency, the magnon resonance temperatures are identified as $T_+ \approx 49$ K for the $+\mathcal{Q}$ mode and $T_- \approx 28$ K for the $-\mathcal{Q}$ mode.

Following this frequency–temperature trajectory, time-domain stroboscopic MOKE mea-

surements are performed. As shown in Fig. 2c, below the conical ordering temperature, the S signals exhibit periodic modulations at the same frequency as the microwave drive, i.e., $\tau = 1/\omega_0 = 312.5$ ps. At a low microwave amplitude of $|\mathbf{H}_{\rm rf}| = 0.066$ mT, characteristic spin resonance features, marked by distinct 'kink' patterns, are observed near 28 K and 49 K [17–19]. These temperatures correspond to T_- and T_+, respectively, in agreement with the frequency-domain results in Fig. 2b. Notably, the observed $S(t_d)$ signals between 30 and 47 K fall within the forced oscillation regime—although ω_0 does not coincide with the system's eigenfrequency, the conical spins are still driven by the time-varying rf field, resulting in a non-zero $M_x(t)$ response.

In contrast, as shown in Fig. 2d, increasing the rf field to $|\mathbf{H}_{\rm rf}| = 0.15$ mT leads to an overall enhancement in the modulation amplitude of the $S(t_d)$ map. However, within the forced oscillation regime (30–47 K), the stroboscopic phases remain unchanged, indicating that the system remains in a passive response mode: the conical spins follow the microwave field without initiating phason motion. At the resonance temperatures T_+ and T_-, by contrast, both the $+\mathcal{Q}$ and $-\mathcal{Q}$ modes exhibit clear phase drifts in $S(t_d)$, signaling the onset of finite-valued Ω_+ and Ω_-, respectively.

This effect becomes particularly evident when comparing two sets of $S(t_d)$ data acquired under the same timescale, as shown in Fig. 2e. At $T_+ = 49$ K, the system enters the $+\mathcal{Q}$ eigenmode. At low microwave power (red curve), $\Omega_+ = 0$, and the conical spin structure remains in a stationary precessional state. However, upon increasing the drive amplitude above the phason threshold (blue curve), a finite Doppler shift in $M_x(t)$ leads to a clear phase offset in the $S(t_d)$ signal. When the temperature is lowered to 38 K, i.e., moving the system out of resonance with the $+\mathcal{Q}$ mode, Ω_+ vanishes and the two $S(t_d)$ profiles become phase-aligned again, confirming the off-resonant nature of the dynamics. A similar signature of phason activation reappears at 29 K, corresponding to the onset of the $-\mathcal{Q}$ eigenmode.

Having established clear experimental evidence for chiral phasons, we next perform systematic investigations of the $|\mathbf{H}_{\rm rf}|$ dependence. Figure 3a presents the stroboscopic MOKE responses measured at various microwave amplitudes under the on-resonance condition for the $+\mathcal{Q}$ magnon mode ($T = 49$ K, $|\mathbf{H}_{\rm dc}| = 40$ mT, $\omega_+ = \omega_0 = 3.2$ GHz). For $|\mathbf{H}_{\rm rf}| < 0.097$ mT, the $S(t_d)$ profiles remain uniform. Increasing the drive amplitude enhances the spin precession amplitude, but $M_x(t)$ retains a single frequency component, i.e., no phason motion is present. At higher microwave powers, the signal exhibits distinct

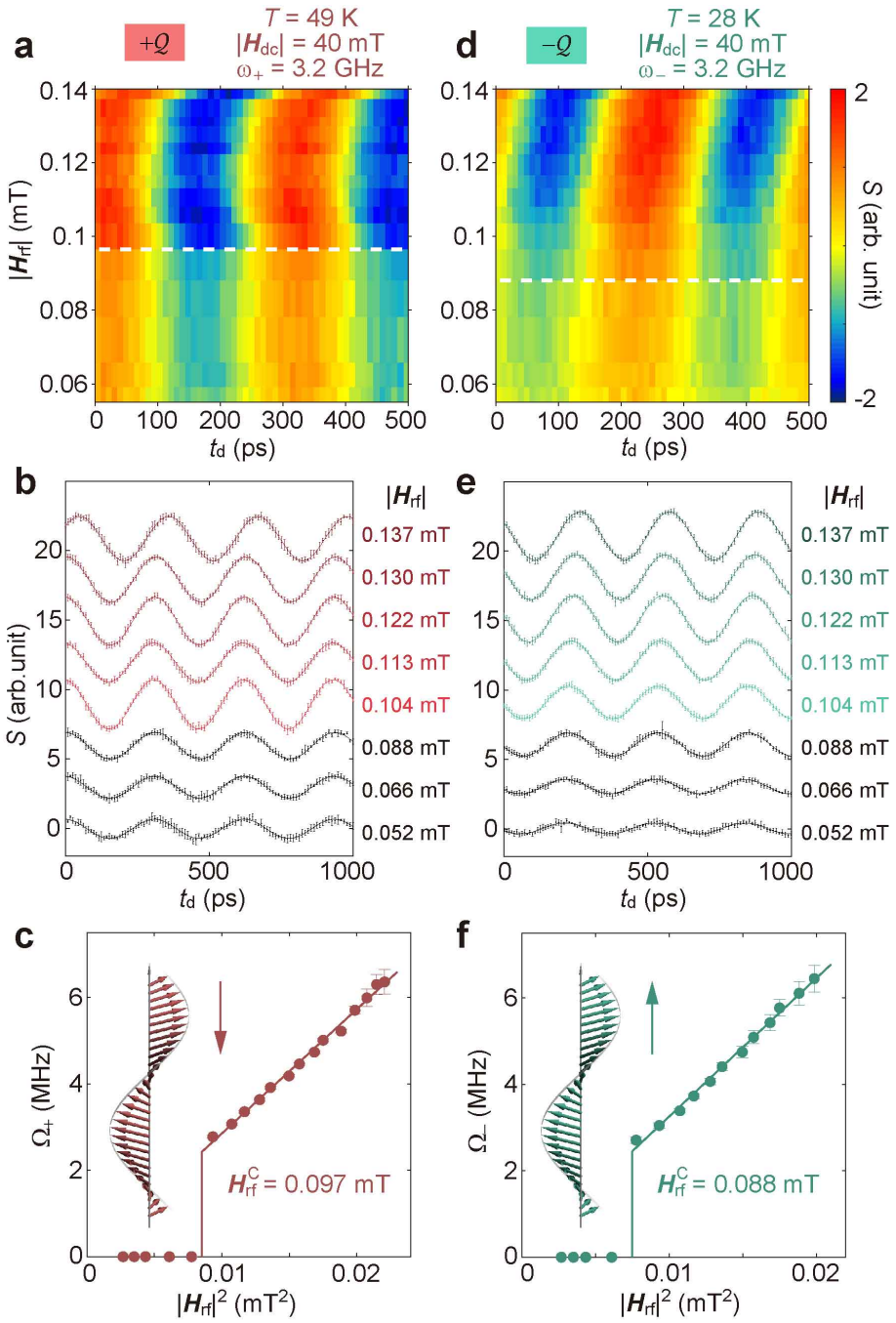

FIG. 3. **Quantitative measurements of chiral phasons.** **a**, $S(t_d)$ signals measured at varying microwave amplitudes under the $+\mathcal{Q}$ resonance condition: $T = 49$ K, $|\mathbf{H}_{\rm dc}| = 40$ mT, and $\omega_+ = \omega_0 = 3.2$ GHz. **b**, Same dataset as in (A), presented in a spectrogram to highlight the well-defined sinusoidal shape of the stroboscopic MOKE responses. Data points (dots with error bars) represent averages over ten repetition sequences; solid lines are fits based on equation (3). **c**, Extracted phason frequency Ω_+ as a function of the microwave power $|\mathbf{H}_{\rm rf}|^2$. Data points with error bars are extracted values; the solid line is a linear fit to the above-threshold data. **d-f**, Corresponding results for the $-\mathcal{Q}$-activated forward-sliding phasons, measured at $T = 28$ K, $|\mathbf{H}_{\rm dc}| = 40$ mT, and $\omega_- = \omega_0 = 3.2$ GHz.

changes in both amplitude and phase, indicating the activation of phason dynamics. Furthermore, as $|\mathbf{H}_{\mathrm{rf}}|$ increases, the modulation pattern evolves continuously, consistent with the expected behavior of an Archimedean screw mode. From this, we identify the threshold amplitude for exciting the backward-sliding phason as 0.097 mT. Figure 3b displays representative $S(t_d)$ traces from Fig. 3a, highlighting their single-harmonic nature and statistical robustness (data points with error bars). The high signal quality enables reliable extraction of Ω_+ by fitting the oscillatory profiles to equation (3), as indicated by the solid lines.

The quantitatively analysis is summarized in Fig. 3c, in which the key features of the backward-sliding phasons are represented by the $\Omega_+(|\mathbf{H}_{\mathrm{rf}}|^2)$ relation. Here, the threshold value $H_{\mathrm{rf}}^{\mathrm{C}}$ is found, below which the conical chain translation motion is pinned by the crystal defects. Once the pinning potential barrier is overcome by greater microwave powers, Ω_+ quadratically increases with $|\mathbf{H}_{\mathrm{rf}}|$. For the present study, Ω_+ reaches $\approx$6 MHz within the experimentally accessible microwave power range, corresponding to a phason velocity of $\approx$0.36 m/s.

On the other hand, excitation of the $-\mathcal{Q}$ magnon mode activates forward-sliding phasons. As shown in Fig. 3d-f, at $T = 28$ K, $|\mathbf{H}_{\mathrm{dc}}| = 40$ mT, and $\omega_- = \omega_0 = 3.2$ GHz, similar dynamical behavior is observed. First, the onset of Ω_- occurs at a threshold microwave amplitude of $H_{\mathrm{rf}}^{\mathrm{C}} = 0.088$ mT, comparable to the Ω_+ case. Second, Ω_- exhibits a quadratic dependence on $|\mathbf{H}_{\mathrm{rf}}|$, reaching values in the few-MHz range. These features are consistent with theoretical expectations (see Fig. 1b).

In summary, we have demonstrated the excitation of magnon-induced phason modes in a conical spin order, thus accessing an unexplored regime of low-energy quasiparticle excitations in magnetic systems. Owing to the screw symmetry of the spin helix, the resulting phase-sliding motion is inherently unidirectional. Above a critical microwave power, chiral phasons can be selectively driven and their propagation velocities can be finely tuned. This collective behavior enables the coherent transport of magnetization density waves, reminiscent of a 'magnon laser' that effectively channels spin angular momentum along a fixed direction. Notably, the MHz-scale phason dynamics introduces simultaneous temporal and spatial periodicity for magnons and electrons, thereby establishing a unique Floquet platform for engineering emergent quantum phases.

Materials and Methods

Materials and methods are summarized in the Supplementary Information [25].

References

[1] S. Shapiro, Josephson currents in superconducting tunneling: the effect of microwaves and other observations, Phys. Rev. Lett. **11**, 80 (1963).

[2] P. Bak and J. von Boehm, Ising model with solitons, phasons, and 'the devil's staircase', Phys. Rev. B **21**, 5297 (1980).

[3] G. Grüner, The dynamics of charge-density waves, Rev. Mod. Phys. **4**, 1129 (1988).

[4] M. Manley, A. May, B. Winn, D. Abernathy, R. Sahul, and R. Hermann, Phason-dominated thermal transport in fresnoite, Phys. Rev. Lett. **129**, 255901 (2022).

[5] S. Kim, Y. Lv, X.-Q. Sun, C. Zhao, N. Bielinski, A. Murzabekova, K. Qu, R. A. Duncan, Q. L. D. Nguyen, M. Trigo, D. P. Shoemaker, B. Bradlyn, and F. Mahmood, Observation of a massive phason in a charge-density-wave insulator, Nat. Mater. **22**, 429 (2023).

[6] H.-H. Yang, L. Desplat, V. P. Kravchuk, M. Hervé, T. Balashov, S. Gerber, M. Garst, B. Dupé, and W. Wulfhekel, Observation of the sliding phason mode of the incommensurate magnetic texture in Fe/Ir(111), npj Quant. Mater. **9**, 54 (2024).

[7] N. del Ser, L. Heinen, and A. Rosch, Archimedean screw in driven chiral magnets, SciPost Phys. **11**, 009 (2021).

[8] P. M. Chaikin and T. C. Lubensky, *Principles of Condensed Matter Physics* (Cambridge University Press, 1995).

[9] C. Pfleiderer, D. Reznik, L. Pintschovius, H. v. Löhneysen, M. Garst, and A. Rosch, Partial order in the non-fermi-liquid phase of MnSi, Nature **427**, 227 (2004).

[10] M. Uchida, Y. Onose, Y. Matsui, and Y. Tokura, Real-space observation of helical spin order, Science **311**, 359 (2006).

[11] S. Mühlbauer, B. Binz, F. Jonietz, C. Pfleiderer, A. Rosch, A. Neubauer, R. Georgii, and P. Böni, Skyrmion lattice in a chiral magnet, Science **323**, 915 (2009).

[12] Y. Togawa, T. Koyama, K. Takayanagi, S. Mori, Y. Kousaka, J. Akimitsu, S. Nishihara,

K. Inoue, A. S. Ovchinnikov, and J. Kishine, Chiral magnetic soliton lattice on a chiral helimagnet, Phys. Rev. Lett. **108**, 107202 (2012).

[13] N. Nagaosa and Y. Tokura, Topological properties and dynamics of magnetic skyrmions, Nat. Nanotech. **8**, 899 (2013).

[14] M. Date, K. Okuda, and K. Kadowaki, Electron spin resonance in the itinerant-electron helical magnet MnSi, J. Phys. Soc. Jpn. **42**, 1555 (1977).

[15] A. Bauer and C. Pfleiderer, Generic aspects of skyrmion lattices in chiral magnets, in *Topological Structures in Ferroic Materials: Domain Walls, Vortices and Skyrmions* (Springer International Publishing, Cham, 2016) pp. 1–28.

[16] N. del Ser and V. Lohani, Skyrmion jellyfish in driven chiral magnets, SciPost Phys. **15**, 065 (2023).

[17] M. Kataoka, Spin waves in systems with long period helical spin density waves due to the antisymmetric and symmetric exchange interactions, J. Phys. Soc. Jpn. **56**, 3635 (1987).

[18] D. Belitz, T. R. Kirkpatrick, and A. Rosch, Theory of helimagnons in itinerant quantum systems, Phys. Rev. B **73**, 054431 (2006).

[19] M. Garst, J. Waizner, and D. Grundler, Collective spin excitations of helices and magnetic skyrmions: review and perspectives of magnonics in non-centrosymmetric magnets, J. Phys. D: Appl. Phys. **50**, 293002 (2017).

[20] D. Kurebayashi, Y. Liu, J. Masell, and N. Nagaosa, Theory of charge and spin pumping in atomic-scale spiral magnets, Phys. Rev. B **106**, 205110 (2022).

[21] Y. Onose, Y. Okamura, S. Seki, S. Ishiwata, and Y. Tokura, Observation of magnetic excitations of skyrmion crystal in a helimagnetic insulator Cu_2OSeO_3, Phys. Rev. Lett. **109**, 037603 (2012).

[22] T. Schwarze, J. Waizner, M. Garst, A. Bauer, I. Stasinopoulos, H. Berger, C. Pfleiderer, and D. Grundler, Universal helimagnon and skyrmion excitations in metallic, semiconducting and insulating chiral magnets, Nat. Mater. **14**, 478 (2015).

[23] C. Doppler, Über das farbige Licht der Doppelsterne und einiger anderer Gestirne des Himmels, Verlag der königl. böhm. Gesellschaft der Wissenschaften **2**, 465 (1842).

[24] I. Neudecker, K. Perzlmaier, F. Hoffmann, G. Woltersdorf, M. Buess, D. Weiss, and C. H. Back, Modal spectrum of permalloy disks excited by in-plane magnetic fields, Phys. Rev. B **73**, 134426 (2006).

[25] See Supplemental Material for more details..

[26] W. Tan, H. Jin, R. Fan, K. Ran, and S. Zhang, Evidence for giant surface Dzyaloshinskii-Moriya interaction in the chiral magnetic insulator Cu_2OSeO_3, Phys. Rev. B **109**, L220402 (2024)

Acknowledgments

This work was supported by the National Key R&D Program of China (Grant no. 2022YFA1403602), the National Natural Science Foundation of China (Grant no. 12241406), and the Double First-Class Initiative Fund of ShanghaiTech University.

Author contributions

All authors discussed and contributed to the manuscript. In particular, Y.W. and H.N.J. conducted the stroboscopic MOKE measurements; J.D.Z. and Y.Z.L. carried out the theoretical studies; C.H.Z. and J.Y.C. performed numerical simulations; S.L.Z. conceived and supervised the project.

Additional information

Supplementary information is available in the online version of the paper. Reprints and permissions information is available online at www.nature.com/reprints. Correspondence and requests for materials should be addressed to S. Zhang.

Competing financial interests

The authors declare no competing financial interests.

Corresponding authors: jinhn1@shanghaitech.edu.cn, liuxp1@shanghaitech.edu.cn,

and shilei.zhang@shanghaitech.edu.cn

Supplementary Files

This is a list of supplementary files associated with this preprint. Click to download.

- SMchiralphasonsv5.pdf
- SM1backward.avi
- SM2forward.avi